Editors' Suggestion

Saturation and coercivity limit the velocity of rotating active magnetic microparticles

Kiarash Samsami, Seyed Amir Mirbagheri, Farshad Meshkati, and Henry Chien Fu*
Department of Mechanical Engineering, University of Utah, Salt Lake City, Utah 84112, USA

(Received 15 January 2020; accepted 6 May 2020; published 8 June 2020)

One class of active particles that is especially promising for biomedical microrobotic applications is rigid magnetic microswimmers propelled via rotation by a magnetic field. For these particles there is a maximum rotational frequency, hence velocity, determined by the maximum torque exerted by the field on the particle magnetization. It has been expected that velocity can always be increased by increasing the field magnitude to increase torque. This expectation holds if magnetization is constant or responds linearly to applied field, but all real materials actually respond nonlinearly, since as field strength increases the magnetization saturates and is coerced to point along the field direction. Here we show that this saturation and coercivity limit the maximum velocity of these microparticles. These effects are particularly important for soft magnetic materials. Although soft magnetic materials are used in many microswimmers, propulsion models incorporating their magnetic response are lacking. Our results are consistent with experimental observations and we predict that the limiting behavior occurs for common magnetic materials at typical rotational frequencies and field strengths, hence is relevant for current microswimmer design.

DOI: 10.1103/PhysRevFluids.5.064202

I. INTRODUCTION

Swimming active microparticles [1] are of great current interest for those creating and studying the properties of new phases of active matter. When capable of controlled navigation, such active particles or microswimmers also become microrobots with applications including drug delivery, microsensing, and micromanipulation [2]. Common types of active particles use different propulsion methods including chemical [3,4], magnetic [5,6], thermal [7], acoustic [8], electric [9,10], and biotic [11–13]. We focus on rigid magnetic microswimmers with nanoscale features that are propelled via rotation by a magnetic field [14–16], which are particularly promising for biomedical microrobotic applications [17]. Over the past decade the dynamics and control of these rigid helical magnetic swimmers has been an active area of study both experimentally and theoretically [17–26].

Most realizations of these microswimmers utilize a rotating uniform magnetic field [17,27] producing on the particle zero external magnetic force, and a magnetic torque that is proportional to both the magnetization and field strength [28]. Usually the magnetic field is perpendicular to its rotation axis [Fig. 1(a)]. The particles can be experimentally controlled by the rotation axis, rotation rate, and magnitude of the field. The average velocity ($\boldsymbol{v}_a$) is along the rotation axis and steering is achieved by setting the rotation axis in a desired direction. Although nonhelical geometries of such microswimmers are an increasing area of interest [21,22,29–32], we specifically consider helical microswimmers to focus on the effects of magnetization. For a fixed field magnitude, the average velocity of helical microswimmers is typically proportional to the rotation rate (frequency) of the

*henry.fu@utah.edu

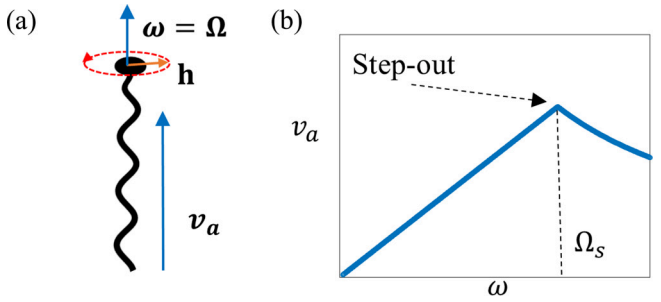

FIG. 1. Schematic of rigid magnetic microswimmer and its velocity-frequency response. (a) Magnetic field $\boldsymbol{h}$ is rotated with an angular velocity $\boldsymbol{\omega}$ resulting in rotation of the swimmer with angular velocity $\boldsymbol{\Omega}$ and average translational velocity $\boldsymbol{v}_a$. (b) Schematic of typical velocity-frequency response for helical magnetic microswimmers. Up to the step-out frequency (Ω_s), the average velocity is proportional to ω.

field up to a certain *step-out* frequency [18], above which there is not enough magnetic torque to rotate the swimmer as fast as the field. The maximum velocity occurs at the step-out frequency and is an important performance metric [32]; the velocity decreases for higher frequencies [Fig. 1(b)]. Assuming that torque increases as magnetic field strength increases leads to the current expectation that step-out frequency and maximum velocity can be increased by increasing the field magnitude.

This expectation holds for microswimmers that are permanent magnets, which have constant magnetization, or paramagnets, which have magnetization that varies linearly with applied field [18,21–24,26], but any real material combines two key features in a way so far unaccounted for: as the applied field increases, the magnetization saturates at a maximum amplitude that depends on the material, and at high enough fields the direction of magnetization tends toward the direction of the applied field. The latter effect occurs through the same physics that causes demagnetization when a strong enough opposing field is applied, so we refer to it by the same name, coercivity. In particular, these effects are important for soft magnetic materials, which have been used in microswimmers [15,27], but there are no models that treat soft magnetic microswimmers. In this paper we show theoretically and numerically that saturation and coercivity impose fundamental physical limits on the performance of magnetically rotated active particles, causing the step-out frequency and hence maximum velocity to approach a constant plateau as field magnitude is increased, rather than increase without bound. This limitation is consistent with experiments, and we predict that it is important in the current design space of microswimmers.

II. PROPULSION MODEL

Active microparticles propelled through bulk fluid by rotating magnetic fields operate in a viscous-dominated regime, in which the external force ($\boldsymbol{F}$) and torque ($\boldsymbol{\tau}$) on a particle are linearly related to its translational ($\boldsymbol{v}$) and angular ($\boldsymbol{\Omega}$) velocities through a 6×6 mobility matrix [22],

$$\begin{bmatrix} \boldsymbol{v} \\ \boldsymbol{\Omega} \end{bmatrix} = \begin{bmatrix} \boldsymbol{K} & \boldsymbol{C} \\ \boldsymbol{C}^T & \boldsymbol{M} \end{bmatrix} \begin{bmatrix} \boldsymbol{F} \\ \boldsymbol{\tau} \end{bmatrix}. \tag{1}$$

The 3×3 submatrices $\boldsymbol{K}$ and $\boldsymbol{M}$ relate the linear and angular velocities to force and torque, respectively, while $\boldsymbol{C}$ relates the linear velocity to the torque and angular velocity to the force (see Table I for our list of symbols).

In a constantly rotated field, "steady" solutions occur when the angular velocity $\boldsymbol{\Omega}$ of the swimmer equals the angular velocity of the field $\boldsymbol{\omega}$ [22] [$\boldsymbol{\Omega} = \boldsymbol{\omega}$; Fig. 1(a)]; i.e., the particle and field rotate together. Then in the particle's body frame the field, magnetization, rotation rate, and velocity are all constant in time, simplifying analysis. Our method for finding steady solutions is described in [22,26] for permanent magnets (constant magnetization). For a given field magnitude

TABLE I. Symbols used in main text.

Symbol	Description
A	magnetic energy anisotropy
$\boldsymbol{C}$	off-diagonal mobility submatrix [Eq. (1)]
$c_{e1-e2,s1-s3}$	model parameters in magnetic anisotropy
δ_{ij}	Kronecker delta
$\delta\alpha_i$	infinitesimal rotation of body
e	magnetic energy
ϵ_{ijk}	antisymmetric Levi-Civita symbol
$\boldsymbol{F}$	external force exerted on swimmer
ϕ	azimuthal angle in spherical coordinates
ϕ_h	azimuthal angle of magnetic field
ϕ_m	azimuthal angle of magnetization
$\boldsymbol{h}$	applied magnetic field
h_c	coercive field strength
$\boldsymbol{K}$	linear mobility submatrix [Eq. (1)]
$\boldsymbol{\chi}$	tensor magnetic susceptibility
$\boldsymbol{\chi}_e$	tensor magnetic susceptibility of ellipsoid
L	arclength of the helical tail
$\boldsymbol{M}$	angular mobility submatrix [Eq. (1)]
$\boldsymbol{m}$	magnetization vector
m_r	remanence
m_s	saturation magnetization
μ_0	permeability of free space
η	dynamic viscosity
R_h	aspect ratio of ellipsoidal head
r_a	minor axis radius of ellipsoidal head
r_b	major axis radius of ellipsoidal head
r_h	radius of helical tail
r_t	radius of thickness of tail
$\boldsymbol{\tau}$	external torque acting on swimmer
θ	polar angle in spherical coordinates
θ_h	polar angle of magnetic field
θ_m	polar angle of magnetization
V	volume of magnetic material
$\boldsymbol{v}$	velocity of swimmer
v_a	time-average velocity of swimmer
$\boldsymbol{\Omega}$	angular velocity of swimmer
$\boldsymbol{\Omega}_s$	angular velocity of swimmer at step-out
$\boldsymbol{\omega}$	angular velocity of magnetic field
ω_s	step-out frequency

and rotation rate, there can exist discrete solutions each with a specific magnetic field direction in the body frame. Steady solutions exist only below the step-out frequency, which is thus determined by the steady solution with maximum $|\boldsymbol{\Omega}|$.

Combining Eq. (1) and the condition $\boldsymbol{F} = 0$,

$$\boldsymbol{v} = \boldsymbol{C}\boldsymbol{M}^{-1}\boldsymbol{\Omega}. \tag{2}$$

Therefore if $\hat{\boldsymbol{\Omega}}$ (hats denote normalized unit vectors) has a fixed direction in the body frame as $|\boldsymbol{\Omega}|$ varies, as is typical for a microswimmer with large aspect ratio [26], then its velocity and hence time-average velocity ($\boldsymbol{v}_a$) will be proportional to frequency, with maximum at the step-out frequency.

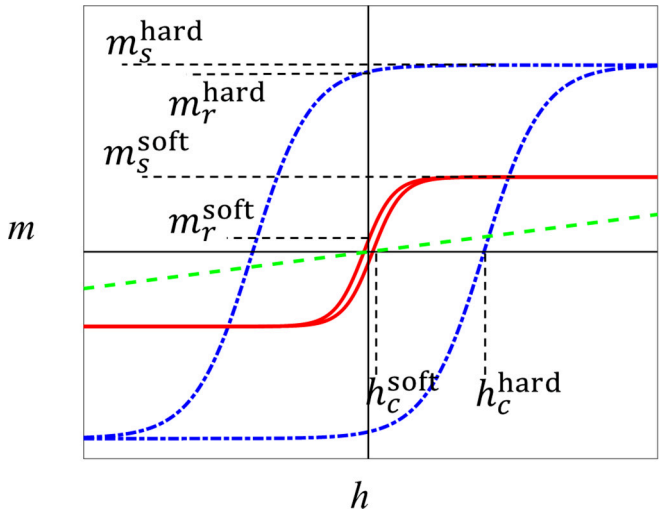

FIG. 2. Types of magnetic materials. Magnetization (m) response to an applied field h for paramagnetic (green dashed line), hard magnetic (blue dot-dashed line), and soft magnetic (red solid line) material. Saturation magnetization (m_s), remanence (m_r), and coercive field (h_c) are indicated for hard and soft magnets.

III. MAGNETIZATION MODEL AND MAGNETIC TORQUE

Different types of magnetization response to applied field can be classified by remanence and coercivity. Remanence (m_r) is how much magnetization remains after removing the applied field. The coercive field (h_c) is the opposing applied field required to demagnetize the material, since the magnetization tends to align with an applied field. Soft ferromagnets (Fig. 2, red solid line) have a magnetization amplitude that increases with increasing field magnitude until it saturates at a constant saturation value m_s. Hard ferromagnets (Fig. 2, blue dot-dashed line) have a magnetization that can be assumed to be constant in typical operational ranges due to their high remanence and coercive field, but in applied fields larger than h_c their magnetization will eventually align with the field. Paramagnetic response (Fig. 2, green dashed line), with magnetization linearly related to the field, is observed for materials with close to zero remanence and coercive field in fields much smaller than those needed to cause saturation. Paramagnets typically have small magnetization compared to ferromagnets.

We develop a phenomenological magnetization model to capture the effects of saturation and coercivity by writing magnetic energy (e) as the sum of a magnetic potential term and an anisotropy term,

$$e = -\mu_0 V \boldsymbol{m} \cdot \boldsymbol{h} + A(\boldsymbol{m}), \tag{3}$$

where m is the magnetization, V is the volume of magnetic material, and μ_0 is the permeability of free space. For a given field, the magnetization is determined by minimizing e with respect to $\boldsymbol{m}$, as appropriate in a quasistatic limit of magnetization dynamics. The choice of A in Eq. (3) can account for different magnetic physics including shape or magnetocrystalline anisotropy.

A paramagnet is described if the anisotropy is $A(\boldsymbol{m}) = \frac{1}{2}\mu_0 V \boldsymbol{m} \cdot \boldsymbol{\chi}^{-1}\boldsymbol{m}$, where $\boldsymbol{\chi}$ is the (symmetric) tensor magnetic susceptibility that depends on the material and geometry of the object. Then minimizing the energy ($\frac{\delta e}{\delta \boldsymbol{m}} = 0$) results in the linear relation $\boldsymbol{m} = \boldsymbol{\chi}\boldsymbol{h}$.

To include saturation, we impose the additional constraint $|\boldsymbol{m}| \leqslant m_s$. Then magnetization responds as a paramagnet in the unsaturated regime but saturates at higher field magnitudes, similar to the experimentally validated description of soft magnetic materials in Ref. [33]. While the small-field unsaturated regime is only well described for materials with small remanence

(i.e., paramagnets and soft magnets), the large-field saturated and coercive regime—the one of importance for the phenomena we investigate—is well described for all types of magnetic materials. For large enough field magnitudes, $|\boldsymbol{m}| = m_s$, the first term on the right-hand side of Eq. (3) becomes dominant, and $\hat{\boldsymbol{m}}$ approaches $\hat{\boldsymbol{h}}$. In the limit $|\boldsymbol{h}| \to \infty$, that first term is minimized by $\hat{\boldsymbol{m}} = \hat{\boldsymbol{h}}$, and for $|\boldsymbol{h}| \gg m_s$ we can find a perturbation expansion

$$\hat{\boldsymbol{m}} = \hat{\boldsymbol{h}} + \frac{m_s \boldsymbol{n}(\hat{\boldsymbol{h}})}{|\boldsymbol{h}|} + O\left(\frac{m_s^2}{|\boldsymbol{h}|^2}, \dots\right), \tag{4}$$

where $\boldsymbol{n}$ is a vector that only depends on the direction, not magnitude, of $\boldsymbol{h}$. As shown in Appendix A, $\boldsymbol{n}$ is the projection of $-\nabla_{\boldsymbol{m}} A/(\mu_0 V m_s)$ into the plane perpendicular to $\hat{\boldsymbol{h}}$. For the following arguments, it is enough that Eq. (4) describes the coercive large-field behavior.

The torque $\boldsymbol{\tau}$ on an object with constant magnetization $\boldsymbol{m}$ and volume V in a magnetic field $\boldsymbol{h}$ is [28]

$$\boldsymbol{\tau} = \mu_0 V \boldsymbol{m} \times \boldsymbol{h}. \tag{5}$$

However, the magnetization determined from Eq. (3) is not constant; it is a function of applied field and the body orientation. For this nonconstant magnetization, we can find the torque on the body using the principle of virtual work by calculating the variation of energy due to variation in body orientation while the field remains fixed. This energy variation due to an infinitesimal rotation of the body ($\delta\alpha_i$) is equivalent to the energy variation due to an opposite rotation of the field ($-\delta\alpha_i$) while the body remains fixed. The energy change due to such a rotation of the field can be written as

$$\delta e = \left(\frac{\partial e}{\partial \boldsymbol{h}} + \frac{\partial e}{\partial \boldsymbol{m}} \frac{\delta \boldsymbol{m}}{\delta \boldsymbol{h}}\right) \delta \boldsymbol{h}. \tag{6}$$

The second term in the parentheses on the right-hand side of Eq. (6) vanishes since $\frac{\partial e}{\partial \boldsymbol{m}} = 0$. Then since the change in field ($\delta \boldsymbol{h}$) due to an infinitesimal rotation $-\delta\alpha_i$ is $\delta h_i = -\epsilon_{ijk} \delta\alpha_j h_k$, we get $\delta e = \mu_0 V \delta\alpha_i \epsilon_{ijk} m_j h_k$, and

$$\tau_i = \frac{\delta e}{\delta \alpha_i} = \mu_0 V (\boldsymbol{m} \times \boldsymbol{h})_i. \tag{7}$$

In the above we use indicial notation with implied summation of repeated indices, and ϵ_{ijk} is the antisymmetric Levi-Civita tensor. Hence in our model the magnetic torque obeys Eq. (5) just as for material with a permanent magnetization.

IV. GENERAL THEORY OF STEP-OUT

Since mobility matrices depend only on the geometry of the particle, Eq. (2) suggests that magnetic properties will not affect the slope of the velocity-frequency response [Fig. 1(b)]. Instead, they greatly affect the behavior of step-out frequency as a function of field magnitude. For a given field magnitude, the step-out frequency is the maximum possible rotation rate of the field that the microswimmer can steadily follow. Working in the body frame, the step-out frequency is obtained by finding the maximum angular velocity value among the steady solutions over varying directions of $\boldsymbol{h}$ while keeping its magnitude constant, or using Eqs. (2) and (5), and the steady condition $\boldsymbol{\omega} = \boldsymbol{\Omega}$,

$$\omega_s = |\boldsymbol{\Omega}_s| = \max_{\hat{\boldsymbol{h}}} \{|\mu_0 V \boldsymbol{M}(\boldsymbol{m}(\boldsymbol{h}) \times \boldsymbol{h})|\}. \tag{8}$$

Step-out for a permanent magnet. If $\boldsymbol{m}(\boldsymbol{h})$ is a constant vector relative to the body, Eq. (8) becomes

$$|\boldsymbol{\Omega}_s| = \max_{\hat{\boldsymbol{h}}} \{\mu_0 V |\boldsymbol{m}||\boldsymbol{h}||\boldsymbol{M}(\hat{\boldsymbol{m}} \times \hat{\boldsymbol{h}})|\}. \tag{9}$$

Since $\boldsymbol{M}$ and $\boldsymbol{m}$ are constant in the body frame, there is a unique direction of $\boldsymbol{h}$ that maximizes the right-hand side, and thus the step-out frequency is linear in $|\boldsymbol{h}|$.

Step-out for a paramagnet. If $\boldsymbol{m}$ is paramagnetic [$\boldsymbol{m}(\boldsymbol{h}) = \boldsymbol{\chi} \cdot \boldsymbol{h}$], Eq. (8) becomes

$$|\boldsymbol{\Omega}_s| = \max_{\hat{\boldsymbol{h}}}\{\mu_0 V |\boldsymbol{h}|^2 |\boldsymbol{M}((\boldsymbol{\chi}\hat{\boldsymbol{h}}) \times \hat{\boldsymbol{h}})|\}. \tag{10}$$

Again, regardless of the field magnitude, a unique direction of $\boldsymbol{h}$ maximizes the right-hand side, but now the step-out increases in proportion to $|\boldsymbol{h}|^2$.

Step-out in the saturated and coercive regime. When the applied field is large enough to saturate and coerce the magnetic response, $|\boldsymbol{m}| = m_s$ and $\hat{\boldsymbol{m}}$ approaches $\hat{\boldsymbol{h}}$. From Eq. (4), $\boldsymbol{m} \times \boldsymbol{h} = m_s^2 \boldsymbol{n}(\hat{\boldsymbol{h}}) \times \hat{\boldsymbol{h}}$, to lowest order, and Eq. (8) becomes

$$|\boldsymbol{\Omega}_s| = \max_{\hat{\boldsymbol{h}}}\{\mu_0 V m_s^2 |\boldsymbol{M}(\boldsymbol{n}(\hat{\boldsymbol{h}}) \times \hat{\boldsymbol{h}})|\}. \tag{11}$$

Since $\boldsymbol{n}$ is independent of $|\boldsymbol{h}|$, we conclude that the step-out frequency will not change for increasing field magnitudes once Eq. (4) is valid. Thus, by going beyond permanent and paramagnetic magnetization to include coercivity and saturation, we see that for a microswimmer made of any real material both the step-out frequency and the maximum velocity plateau when the field magnitude becomes large enough. Physically, the origin of this plateau behavior is that as $|\boldsymbol{h}|$ increases, the angle between $\boldsymbol{m}$ and $\boldsymbol{h}$ decreases proportionally to $\frac{1}{|\boldsymbol{h}|}$, and hence the torque $\boldsymbol{\tau} = \mu_0 V \boldsymbol{m} \times \boldsymbol{h}$ remains constant.

V. NUMERICAL DEMONSTRATION OF PLATEAU BEHAVIOR

Next we numerically demonstrate the described step-out behavior by modeling a microswimmer with a helical tail and prolate ellipsoidal head [Fig. 3(a)].

A. Model for microswimmer with ellipsoidal head

The magnetization response of an ellipsoidal head is relatively simple, with a single easy axis, and we choose a specific anisotropy [$A(\boldsymbol{m})$ in Eq. (3)] to capture the shape anisotropy of a soft magnetic prolate ellipsoid with randomly oriented domains.

The axial symmetry of the ellipsoid constrains the magnetic properties. First, the magnetization always lies in the same plane as the field and axis of symmetry [$\phi_m = \phi_h$; Fig. 3(a)]. Second, the anisotropy expression should be independent of the azimuthal angle ϕ_m and only be a function of polar angle θ_m. Third, since the major axis of a prolate ellipsoid is its easy axis, $A(\boldsymbol{m})$ should be symmetric around $\theta_m = \pi/2$, with minima at $\theta_m = 0, \pi$ and a maximum at $\theta_m = \pi/2$. An anisotropy satisfying these properties is

$$A(\boldsymbol{m}) = \tfrac{1}{2}\mu_0 V \boldsymbol{m} \cdot \boldsymbol{\chi}_e^{-1} \boldsymbol{m}, \tag{12}$$

where $\boldsymbol{\chi}_e$ is a diagonal matrix of the form

$$\boldsymbol{\chi}_e = \begin{bmatrix} \frac{1}{c_{e1}} & 0 & 0 \\ 0 & \frac{1}{c_{e1}} & 0 \\ 0 & 0 & \frac{1}{c_{e2}} \end{bmatrix}. \tag{13}$$

For a general ellipsoid c_{e1} and c_{e2} are computed in [34] as a function of the ratio of major and minor axes and satisfy the constraint $2c_{e1} + c_{e2} = 1$. For a prolate ellipsoid $c_{e1} > c_{e2}$, which minimizes the energy at $\theta_h = 0, \pi$ and maximizes it at $\theta_h = \pi/2$. For an oblate ellipsoid $c_{e1} < c_{e2}$.

Using Eq. (12) with $\phi_m = \phi_h$, Eq. (3) becomes

$$e = -\mu_0 V\big[|\boldsymbol{m}||\boldsymbol{h}| \cos(\theta_h - \theta_m) + \tfrac{1}{2}|\boldsymbol{m}|^2 (c_{e2} \cos^2\theta_m + c_{e1} \sin^2\theta_m)\big]. \tag{14}$$

Minimizing Eq. (14) under the constraint $|\boldsymbol{m}| \leqslant m_s$ gives the magnetization as $\boldsymbol{m} = \boldsymbol{\chi}\boldsymbol{h}$ for the linear regime where $|\boldsymbol{m}| < m_s$, and as the solution of $(c_{e1} - c_{e2}) m_s \sin(2\theta_m) = 2|\boldsymbol{h}| \sin(\theta_h - \theta_m)$ for the saturated regime where $|\boldsymbol{m}| = m_s$. This magnetization is in agreement with the experimentally

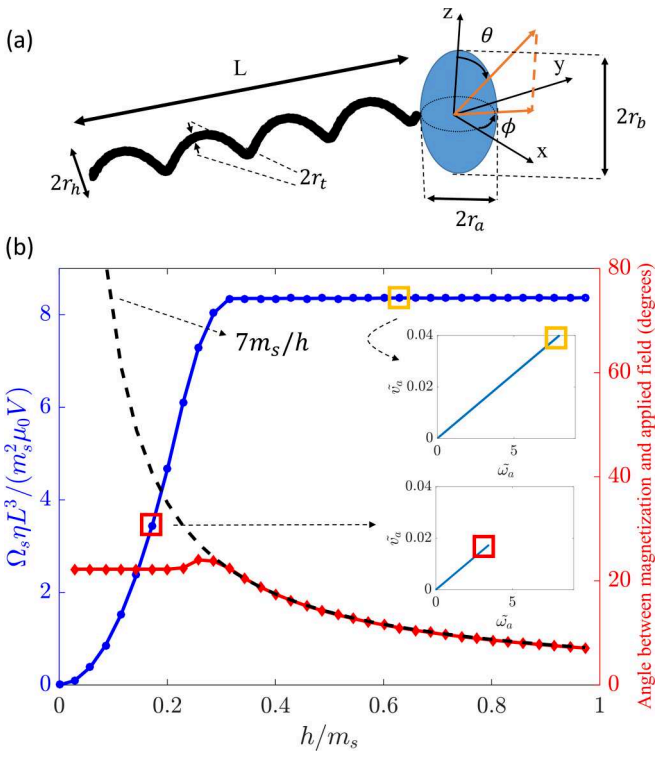

FIG. 3. (a) Schematic of microswimmer with a prolate ellipsoidal head. The volume of magnetic material (V) is not shown, and the head and tail are not to scale. Polar and azimuthal angles θ and ϕ are used to describe vectors in the swimmer's body frame. (b) Demonstration of plateau behavior due to saturation and coercivity for microswimmer with head aspect ratio 2. Nondimensional step-out frequency (Ω_s; left axis) plateaus as field magnitude (h) increases, because the magnetization approaches the field direction, as shown by the angle between magnetization and applied field (right axis). Dashed line shows h^{-1} behavior of this angle. Insets show how step-out frequencies are determined from the largest nondimensional average velocity ($\tilde{v}_a = \frac{v_a \eta L^2}{\mu_0 m_s^2 V}$) and nondimensional frequency ($\tilde{\omega} = \frac{\omega \eta L^3}{\mu_0 m_s^2 V}$) for which a solution exists, where η is the dynamic viscosity of the fluid.

validated model proposed in [33]; our coefficients c_{e1} and c_{e2} correspond to the demagnetization factors there.

To apply the propulsion model (Sec. II), first the submatrices $\boldsymbol{K}$, $\boldsymbol{C}$, and $\boldsymbol{M}$ in Eq. (1) are computed using the method of regularized Stokeslets [35] as described in Appendix B. We find steady solutions ($\boldsymbol{\Omega} = \boldsymbol{\omega}$) for varying field strength and rotation rate using the method described in [22], but must adjust it for the soft magnetic model as follows.

Recall that we compute the field directions (in the swimmer's body frame) resulting in steady orbits. Since for an ellipsoid the field, magnetization, and axis of symmetry are coplanar, for a field direction described in body frame as $\hat{\boldsymbol{h}} = [\sin\theta_h \cos\phi_h, \sin\theta_h \sin\phi_h, \cos\theta_h]$, the torque [Eq. (7)] lies in the x-y plane,

$$\hat{\boldsymbol{\tau}} = \begin{bmatrix} -\sin\phi_h \\ \cos\phi_h \\ 0 \end{bmatrix}. \tag{15}$$

The angle between rotation axis of the field and the field itself is prescribed experimentally and in this paper it is assumed that they are perpendicular as is typical in experiments. Hence $\hat{\boldsymbol{h}} \cdot (\boldsymbol{M}\hat{\boldsymbol{\tau}}) = 0$ is a constraint that can be used to determine the steady solutions. This constraint results in

$$\tan\theta_h = \frac{M_{13}\sin\phi_h - M_{23}\cos\phi_h}{M_{12}\cos 2\phi_h + (M_{22} - M_{11})\sin\phi_h\cos\phi_h}. \tag{16}$$

In a given field magnitude, for each pair of (θ_h, ϕ_h) that solves Eq. (16) we compute the magnetization, then the torque on the swimmer from Eq. (7), and the swimmer's angular velocity $\boldsymbol{\Omega}$ from Eq. (1). Stability for the solutions was confirmed by checking that perturbations return to the original solution under time evolution by numerical integration of the angular velocity in Eq. (1), which agrees with analytical criteria for stability [36].

B. Demonstration of plateau behavior

The insets in Fig. 3(b) show the nondimensional average velocities of steady solutions as a function of nondimensional frequency for $h = 0.17m_s$ and $h = 0.63m_s$; the step-out frequency corresponds to the largest velocities in each plot. Changing the field strength yields the same slope but different step-out frequencies and maximum velocities. The resulting dependence of step-out frequency on field magnitude is shown in Fig. 3(b) (blue circles, left axis). Initially, as field magnitude increases the step-out frequency grows quadratically, corresponding to the regime where coercivity is important but saturation is not yet reached. Since our model assumes a paramagnetic response in this regime, the quadratic behavior is the same as expected for a paramagnet. However, for high field magnitudes the step-out frequency plateaus, confirming our analytical results. Furthermore, the angle between the field and magnetization decreases proportionally to $1/|\boldsymbol{h}|$ as the step-out plateaus [Fig. 3(b), red diamonds, right axis], confirming our physical picture of the origin of plateau behavior.

VI. EXPERIMENTAL RELEVANCE OF PLATEAU BEHAVIOR

To our knowledge, the plateau behavior has not been reported in experiments. Hard magnets are not operated in the coercive regime (by definition) so we do not expect plateau behavior for microswimmers made of those materials.

A. Consistency with reported soft magnetic microswimmer

To check whether our predictions are consistent with existing soft magnetic microswimmers, we model the velocity-frequency response for the soft magnetic swimmer reported in Ref. [15] with a square, not ellipsoidal, head. For this microswimmer, the properties of the anisotropy energy $A(\boldsymbol{m})$ are dictated by a square's geometry and the placement of its easy axis. In agreement with [15], Ref. [37] reports that the easy axis for thin square plates are the diagonals for fields less than $11m_s$. Assuming that holds true, then $A(\boldsymbol{m})$ should be symmetric about $\theta_m = \pi/2$ [Fig. 4(a)] in the range of $0 \leqslant \theta_m \leqslant \pi$ with a minimum at $\theta_m = \pi/2$ and maxima at $\theta_m = 0, \pi$. Also $A(\boldsymbol{m})$ should be 4-fold symmetric with respect to ϕ_m in the range of $0 \leqslant \phi_m \leqslant 2\pi$ with minima at $\phi_m = k_1\pi/2$, $(k_1 = 0, 1, 2, 3, \ldots)$ and maxima at $\phi_m = k_2\pi/4$ $(k_2 = 1, 3, 5, \ldots)$. Adding an additional term to the shape anisotropy of an oblate ellipsoid generates the following anisotropy which satisfies these properties:

$$A(\boldsymbol{m}) = \tfrac{1}{2}\mu_0 V\left[c_{s1}\left(m_x^2 + m_y^2\right) + c_{s2}m_z^2 + c_{s3}m_x^2 m_y^2\right], \tag{17}$$

where c_{s1}, c_{s2}, and c_{s3} are constant coefficients; the first two describe the shape anisotropy of an oblate ellipsoid ($c_{s1} < c_{s2}$), while the third term controls the in-plane behavior of magnetization for a thin square plate with easy axes along its diagonals (the x and y axes). An example of the calculation of the magnetization from this shape anisotropy is presented in Appendix C.

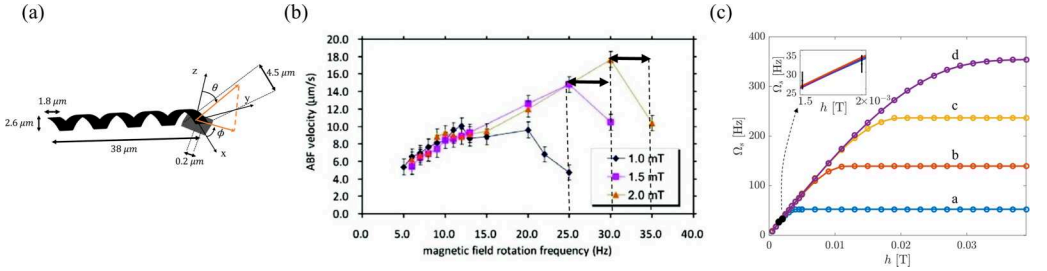

FIG. 4. Plateau behavior of experimental microswimmer with square head. (a) Geometry of microswimmer with a thin square plate head [27]. Polar and azimuthal angles θ and ϕ are used to describe vectors in the swimmer's body frame. (b) Experimental data for velocity versus frequency in three different field magnitudes, with uncertainty in estimation of step-out frequencies indicated. Taken from [27] and modified with permission. (c) Calculated step-out frequencies versus field magnitude for various parameter values as discussed in the main text. Table II shows values of c_{s1}, c_{s2}, c_{s3}, m_s, and E corresponding to each plot. The inset shows more clearly the estimated experimental values of $\omega^e_{1.5}$ and ω^e_2 and their uncertainties relative to our predictions.

Unlike the microswimmer with the ellipsoidal head, we could not derive an analytical expression for the steady solutions ($\boldsymbol{\Omega} = \boldsymbol{\omega}$) for this microswimmer from Eq. (1). Instead, for a given field magnitude, we numerically search for field directions and their resulting angular velocities for which the angle between the two (γ) is close to 90°. We use a threshold of $|\gamma - 90°| \leqslant 1°$ for our simulations but smaller thresholds are possible at the cost of more computation time. In Eq. (1), we require the mobility matrices which are computed using the method of regularized Stokeslets as described in Appendix C.

Prediction of plateau value for reported microswimmer. Reference [27] reports velocities of their experimental microswimmer as a function of frequency for 1, 1.5, and 2 mT fields [Fig. 4(b)]. We estimated the step-out frequency for the 1.5 and 2 mT curves in Fig. 4(b) to be $\omega^e_{1.5} = 27.5$ and $\omega^e_2 = 32.5$ Hz with a ± 2.5 Hz uncertainty. We did not use the 1 mT curve since the uncertainty in approximating the step-out frequency in that field is much larger. To model the experiment, we must specify values for the parameters c_{s1}, c_{s2}, c_{s3}, m_s. We numerically searched for parameters that produce step-out frequencies ($\omega_{1.5}$ and ω_2) at 1.5 mT and 2 mT field magnitudes that locally minimize the error $E = \sqrt{(\omega_{1.5} - \omega^e_{1.5})^2 + (\omega_2 - \omega^e_2)^2}$. We found many such sets of parameters within the experimental uncertainty ($E \leqslant 2.5\sqrt{2}$ Hz).

Four examples are shown in Fig. 4(c) for sets of parameters listed in Table II. The fit constrains m_s within a relatively small range of $(1.9\text{–}2.2) \times 10^4$ A m^{-1}; in Appendix C we check that the implied value for m_s is reasonable for the magnetic structure in this microswimmer. The fit does not strongly confine the values of c_{s1}, c_{s2}, and c_{s3}. The result for c_{s3} can be rationalized since it controls the in-plane behavior of magnetization; however for this microswimmer, magnetization vectors of the steady solutions have in-plane components mostly along the x easy axis. This implies that c_{s3} can change in a wide range without having a strong effect on the step-out curve. In general a wide range of c_{s1} and c_{s2} can fit the data, and larger c_{s2} leads to larger plateau step-out frequencies, which

TABLE II. Values of parameters used in the four curves in Fig. 4(c).

	c_{s1}	c_{s2}	c_{s3} (m^2 A^{-2})	m_s (A m^{-1})	E (Hz)
a	0.0108	0.2102	2.96×10^{-10}	21818	2.09
b	0.001	0.6430	3×10^{-8}	19800	2.50
c	0.004	1.1322	1.23×10^{-5}	19470	2.50
d	0.0082	1.6758	1.74×10^{-11}	19654	2.49

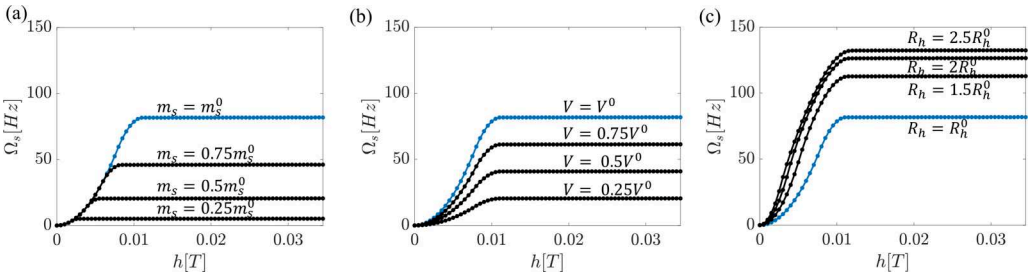

FIG. 5. Effect of material and geometry on plateau behavior. Dependence of step-out frequency (Ω_s) on applied field magnitude (h) for labeled values of (a) saturation magnetization m_s, (b) volume of magnetic material V, and (c) head aspect ratio R_h. h_0, m_s^0, V^0, and R_h^0 are the values for the baseline case (blue curves) described in the text.

also vary over a wide range from 50 Hz to 350 Hz. (Note that even by conservative estimates these microswimmers will remain in the assumed viscously-dominated regime, with Reynolds number less than 0.1, for frequencies of up to a few thousand Hz.) Therefore, while our models are consistent with the experimental data at low frequencies, we are not able to predict the expected plateau behavior for this microswimmer.

B. Plateau behavior is predicted for microswimmers made of common materials in typical operating ranges

Next, to see whether the plateau behavior should be seen in real active particles, we examined the effects of head geometry and material. Using the models for a microswimmer with ellipsoidal head above, we examine the effects of varying saturation magnetization m_s, volume of magnetic material V, and head aspect ratio R_h. As a baseline for comparison, in each case we include a microswimmer (results plotted in blue) consisting of a prolate ellipsoid head of aspect ratio $R_h^0 = 2$ with minor and major radii $r_a = 0.78$ μm and $r_b = 1.56$ μm containing a volume $V^0 = 4.05$ μm^3 of magnetic material with $m_s^0 = 2.78 \times 10^4$ A m^{-1}, and a left-handed helical tail with length $L = 38$ μm, helical radius $r_h = 1.4$ μm, 4.5 turns, and thickness radius of $r_t = 0.7$ μm. This tail geometry (chirality, length, number of turns, and radius) and head volume are chosen to be similar to the experimental microswimmer in [15]. The thickness of the tail relative to the head size is similar to the microswimmer reported in [18]. The saturation magnetization is that of the soft magnetic alloy YIG [37].

First, materials with smaller saturation magnetization lead to smaller plateau step-out frequencies and fields. In Fig. 5(a) we change the value for m_s to represent different magnetic materials while keeping the geometry of the particle constant. As implied by the nondimensionalization in Fig. 3(b), the field strength at which the plateau behavior starts increases linearly with increasing m_s. The plateau step-out frequency increases quadratically with increasing m_s. We note that changing the magnetic material of the head from nickel ($m_s = 4.9 \times 10^5$ A m^{-1} [38]) to YIG ($m_s = 2.78 \times 10^4$ A m^{-1}) decreases the plateau step-out frequency from $\omega_c = 2.7 \times 10^4$ Hz starting at 150 mT, to approximately 100 Hz starting at 10 mT; both values are well outside typical ranges used in experiments. However, as discussed in Appendix C, soft magnetic materials incorporating diamagnetic and/or antiferromagnetic components can have significantly smaller saturation magnetizations than nickel.

Second, decreasing the volume of magnetic material (V) will decrease the plateau step-out frequency. In Fig. 5(b) we decrease the volume of magnetic material while keeping the head geometry constant, as might occur if the magnetic material were a coating rather than the entire head. The plateau step-out frequency is proportional to the magnetic material volume, while the field magnitude at which the plateau starts remains constant. More generally as implied by the

nondimensionalization in Fig. 3(b), the plateau step-out frequency is proportional to the ratio of V and the geometric volume of the swimmer. Thus if a microswimmer is fabricated with a coating of magnetic material of constant thickness, increasing the particle size decreases the ratio of magnetic volume to geometric volume, leading to smaller plateau step-out frequencies and velocities.

Third, the head shape will affect the plateau step-out frequency. In Fig. 5(c) we change the head aspect ratio while keeping the head volume constant. The head aspect ratio affects the magnetization model [Eq. (12)] as well as the mobility matrix [Eq. (1)]. The plateau step-out frequency decreases as the head aspect ratio decreases, but the field magnitude at which the plateau starts remains approximately constant.

Applying these results to realistic materials and geometries, we found that if the microswimmer head of Fig. 3(a) were made from nickel, due to its relatively large saturation magnetization ($m_s = 4.9 \times 10^5$ A m^{-1} [38]), the plateau step-out frequency and the field magnitude at which it happens would be well outside typical laboratory ranges. However, an active particle can easily be designed with experimentally relevant step-out plateau behavior. As a concrete example, we combine all the effects above and model a microswimmer consisting of a prolate ellipsoidal head with minor and major radii $r_a = 1.46$ μm and $r_b = 3.02$ μm, with an additional coating of a 100 nm thick layer of YIG ($m_s = 2.78 \times 10^4$ A m^{-1} [37]), and a left-handed helical tail with 4.5 turns and length $L = 76$ μm, thickness radius $r_t = 1.4$ μm, and helical radius $r_t = 2.8$ μm. We find that the plateau behavior begins at field magnitude of approximately 10 mT, with step-out frequency 12 Hz, and swimming velocity 31 μm s^{-1}, which are well within standard operating ranges for these types of magnetic active particles.

VII. DISCUSSION

We have shown that for active magnetic microswimmers propelled by a rotating magnetic field, previously ignored saturation and coercive effects cause the step-out frequency, and hence maximum velocity, to plateau rather than increase as field magnitude increases. We predict that for reasonable choices of soft magnetic materials and geometry, the plateau in step-out frequency can occur at field magnitudes and rotation rates typically encountered in the laboratory, so this new physical limit is relevant for current microswimmer design.

At low field strengths, our magnetization model assumed paramagnetic behavior. This assumption holds for ideal soft magnetic materials such as HyMu 80 [33], but may not be valid for materials with significant remanence, and quantitative treatment of such materials will require further work. However, our model adequately treats saturation and coercivity for large fields and the limiting behavior is quite general, since it only requires that the saturated magnetization approaches the applied field direction as $(1/|h|)$ as field strength increases [Eq. (4)], which results from any anisotropy $A(\boldsymbol{m})$ independent of $|\boldsymbol{h}|$.

If undesired, the plateau behavior we have identified can easily be avoided by using materials such as nickel with high saturation magnetizations. However, it may also turn out to be advantageous to design microswimmers that can operate in the plateau regime; for example, control of microrobots, especially in swarms, could be achieved using nonlinear response [22,39,40] including post-step-out frequency properties [41] so it may be favorable to have a small step-out frequency. Nonuniform magnetic fields can also be used to control swarms [42], so it may be favorable to have microswimmers with a constant step-out frequency across varying magnetic field strengths.

We considered rigid magnetic particles propelled in bulk fluids, but other types of active particles may be affected by the physical constraint on steady rotation rates we have identified. For instance, magnetic particles are often rotated to roll along surfaces and boundaries [6,43–45], and magnetic rotational actuation is also used in self-assembled micromachines [46]. Finally, limits on maximum rotation rates may also constrain nonpropulsive applications of magnetic particles such as microrheology [47], targeted control of living cells [48], and thermal and mechanical treatment of cancer tumors [49,50].

ACKNOWLEDGMENTS

We thank the University of Utah Center for High Performance Computing for computational support and Jake Abbott for useful discussions and comments. This work was funded by NSF Awards No. CMMI-1650968, No. CBET-1252182, and No. CBET-1805847.

APPENDIX A: LARGE-FIELD PERTURBATION EXPANSION FOR MAGNETIZATION

A nondimensional version of the energy in Eq. (3) for a saturated soft magnet is

$$\tilde{e} = -\hat{\boldsymbol{m}} \cdot \hat{\boldsymbol{h}} + \frac{m_s}{|\boldsymbol{h}|}\tilde{A}(m_s\hat{\boldsymbol{m}}), \tag{A1}$$

where $\tilde{e} = \frac{e}{\mu_0 V m_s |\boldsymbol{h}|}$ and $\tilde{A} = \frac{A}{\mu_0 V m_s^2}$. For $|\boldsymbol{h}| \gg m_s$ Eq. (A1) is minimized by $\hat{\boldsymbol{m}} = \hat{\boldsymbol{h}}$, so for large $\frac{|\boldsymbol{h}|}{m_s}$ we use a perturbation expansion

$$\hat{\boldsymbol{m}} = \frac{\hat{\boldsymbol{h}} + \frac{m_s}{|\boldsymbol{h}|}\boldsymbol{n}(\hat{\boldsymbol{h}}) + \left(\frac{m_s}{|\boldsymbol{h}|}\right)^2 \boldsymbol{n}_1(\hat{\boldsymbol{h}}) + O\left(\left(\frac{m_s}{|\boldsymbol{h}|}\right)^3, \dots\right)}{\sqrt{1 + 2\frac{m_s}{h}\boldsymbol{n}\cdot\hat{\boldsymbol{h}} + \left(\frac{m_s}{h}\right)^2(\boldsymbol{n}^2 + 2\boldsymbol{n}_1\cdot\hat{\boldsymbol{h}}) + O\left(\left(\frac{m_s}{|\boldsymbol{h}|}\right)^3, \dots\right)}}. \tag{A2}$$

This can be further expanded neglecting the $O((\frac{m_s}{|\boldsymbol{h}|})^3, \dots)$ terms to get

$$\begin{aligned}\hat{\boldsymbol{m}} = \hat{\boldsymbol{h}}\left[1 - \frac{m_s}{h}\boldsymbol{n}\cdot\hat{\boldsymbol{h}} - \frac{1}{2}\left(\frac{m_s}{h}\right)^2(\boldsymbol{n}^2 + 2\boldsymbol{n}_1\cdot\hat{\boldsymbol{h}}) + \frac{3}{2}\left(\frac{m_s}{h}\boldsymbol{n}\cdot\hat{\boldsymbol{h}}\right)^2\right] \\ + \left(\frac{m_s}{h}\right)\boldsymbol{n}\left[1 - \left(\frac{m_s}{h}\right)\boldsymbol{n}\cdot\hat{\boldsymbol{h}}\right] + \left(\frac{m_s}{h}\right)^2\boldsymbol{n}_1.\end{aligned} \tag{A3}$$

Substituting Eq. (A3) into Eq. (A1) and minimizing $\tilde{e}$ with respect to $\boldsymbol{n}$,

$$\frac{\partial\tilde{e}}{\partial n_i} = \left(\frac{m_s}{h}\right)^2(\delta_{ij} - \hat{h}_i\hat{h}_j)n_j + \left(\frac{m_s}{h}\right)^2 m_s\frac{\partial\tilde{A}}{\partial m_i}(\delta_{ij} - \hat{h}_i\hat{h}_j) = 0, \tag{A4}$$

which results in

$$(\delta_{ij} - \hat{h}_i\hat{h}_j)\left(n_i + m_s\frac{\partial\tilde{A}}{\partial m_i}\right) = 0. \tag{A5}$$

In the above we use indicial notation with implied summation of repeated indices. Equation (A5) gives the components of $\boldsymbol{n}$ in the plane perpendicular to $\hat{\boldsymbol{h}}$. In the main text, we write the leading order in $\frac{m_s}{h}$ expression for $\hat{\boldsymbol{m}}$, in which we assume $\boldsymbol{n}$ has no component along $\hat{\boldsymbol{h}}$, so that $\hat{\boldsymbol{m}}$ is a unit vector to leading order in $\frac{m_s}{h}$.

APPENDIX B: MOBILITY MATRIX FOR A HELICAL MICROSWIMMER WITH AN ELLIPSOIDAL HEAD

To compute the mobility matrix, we used the method of regularized Stokeslets [35], which represents the flow around a body as a superposition of flows arising from "blobs" of force located at discretized points on the surface of the body. Each blob of force has dimensions specified by a regularization parameter. Figure 6 shows a discretization of the head and tail surfaces for this microswimmer. We discretized the surface of the ellipsoidal head by defining cross sections along the axis of symmetry and putting equally spaced points on the perimeter of each cross section. The number of points on each cross section is chosen so that the spacing between them is as close as possible to the distance between neighboring cross sections. The values of the mobility matrix of the head itself were in good agreement with analytical values of mobility matrix components for an ellipsoid [51]. We discretized the surface of the tail by defining cross sections along the centerline and perpendicular to it and putting points on the perimeter of each cross section. Similarly

FIG. 6. Surface discretization of microswimmer with ellipsoidal head. To scale, 2091 total discretization points.

to the head, the distance between neighboring points on a cross section is equal to the distance between neighboring cross sections. Each tail cross section has the same number of points and any two neighboring cross sections are rotated compared to each other by half the angle between two neighboring points of a cross section so that points are more equally distributed. We chose the regularization parameter for both the head and the tail to be equal to the defined cross-section distance of the head and tail, respectively. The distance between cross sections of the tail is equal to that of the head and we increase the number of discretization points by decreasing this distance. To make sure that the obtained values converge, we compute mobility matrix values [Eq. (1)] as we increase the number of discretization points and compare the percentage change in values of $||\boldsymbol{K}||$, $||\boldsymbol{C}||$, and $||\boldsymbol{M}||$ at each step (where $||\boldsymbol{A}|| = \sqrt{\sum_{ij} A_{ij}A_{ij}}$) until the percentage change between the last three computations is less than 1%.

For the baseline example associated with Fig. 5, the total number of discretization points is 11 358, with 10 605 for the tail and 753 for the head. The values for submatrices $\boldsymbol{K}$, $\boldsymbol{C}$, and $\boldsymbol{M}$ are

$$\boldsymbol{K} = \begin{bmatrix} 2.1080 & 0.0075 & 0.0004 \\ 0.0075 & 1.0310 & 0.0115 \\ 0.0004 & 0.0115 & 2.1644 \end{bmatrix} \times 10^{7}\ \mathrm{N^{-1}\,s^{-1}\,m}, \tag{B1}$$

$$\boldsymbol{C} = \begin{bmatrix} 0.0252 & 0.05058 & 7.0742 \\ -0.0826 & -2.1809 & 0.0728 \\ -7.2956 & 0.7632 & 0.0094 \end{bmatrix} \times 10^{11}\ \mathrm{N^{-1}\,s^{-1}}, \tag{B2}$$

$$\boldsymbol{M} = \begin{bmatrix} 0.0380 & -0.0077 & 0.0001 \\ -0.0077 & 1.0877 & -0.0013 \\ 0.0001 & -0.0013 & 0.0371 \end{bmatrix} \times 10^{18}\ \mathrm{N^{-1}\,s^{-1}\,m^{-1}}. \tag{B3}$$

APPENDIX C: MICROSWIMMER WITH SQUARE HEAD

Example of magnetization calculation for square head. The magnetization is found by numerically minimizing the magnetic energy [Eq. (3)] using the anisotropy Eq. (17) under the constraint that $|\boldsymbol{m}| \leqslant m_s$. For a given field $\boldsymbol{h}$ we compute the magnetization by searching for $|\boldsymbol{m}|$, θ_m, and ϕ_m that minimizes the energy as follows. First we derive an expression for $|\boldsymbol{m}|$ in terms of the known parameters ($\boldsymbol{h}$, c_{s1}, c_{s2}, c_{s3}) and the unknown θ_m and ϕ_m by setting $\frac{\partial e}{\partial |\boldsymbol{m}|} = 0$. This results in

$$\begin{aligned} 0 = &-|\boldsymbol{h}|\{\cos(\theta_m - \theta_h) + \sin\theta_m \sin\theta_h[\cos(\phi_m - \phi_h) - 1]\} \\ &+ |\boldsymbol{m}|[c_{s2}\cos^2(\theta_m) + c_{s1}\sin^2(\theta_m)] + 2c_{s3}|\boldsymbol{m}|^3 \sin^4(\theta_m)\sin^2(\phi_m). \end{aligned} \tag{C1}$$

Since both coefficients of $|\boldsymbol{m}|$ and $|\boldsymbol{m}^3|$ are greater than or equal to zero, Eq. (C1) is monotonic and will always have one real solution $|\boldsymbol{m}| = m'(\phi_m, \theta_m)$. The magnetization must satisfy the soft magnetic constraint of $|\boldsymbol{m}| \leqslant m_s$, hence the actual value of $|\boldsymbol{m}|$ is

$$\tilde{m}(\phi_m, \theta_m) = \min\left(m'(\phi_m, \theta_m), m_s\right). \tag{C2}$$

We then numerically minimize the energy equation with the substitution $|\boldsymbol{m}| = \tilde{m}(\phi_m, \theta_m)$ and the anisotropy modeled for a square [Eq. (17)],

$$e = \mu_0 V\Big[- \tilde{m}\hat{\boldsymbol{m}} \cdot \boldsymbol{h} + \tfrac{1}{2}\tilde{m}^2(c_{s1}\sin^2\theta_m + c_{s2}\cos^2\theta_m) + \tfrac{1}{2}\tilde{m}^4 c_{s3}\sin^4\theta_m \sin^2\phi_m \cos^2\phi_m\Big]. \tag{C3}$$

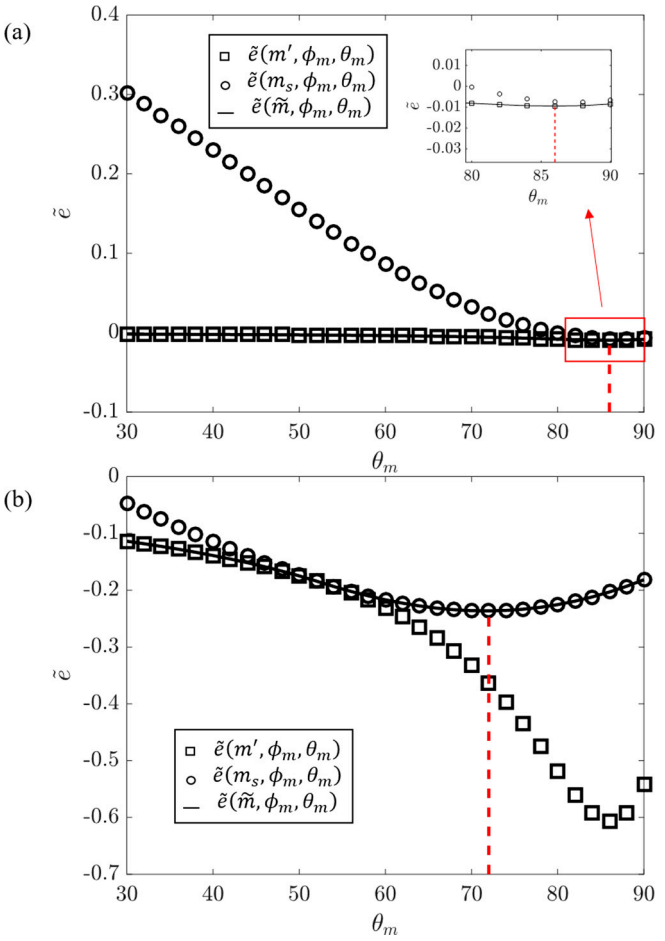

FIG. 7. Example of determination of magnetization with saturation condition. Dimensionless magnetic energy ($\tilde{e} = e/\mu_0 V m_s^2$) for a square for different magnetization directions in an applied field with $\theta_h = 30^\circ$ and $\phi_h = 0$. Square points show energy computed with $|\boldsymbol{m}| = m'$ from Eq. (C4), and the circles show energy computed with $|\boldsymbol{m}| = m_s$. The actual energy values (solid line) are computed with $|\boldsymbol{m}| = \tilde{m}$; see text. (a) Field magnitude is $|\boldsymbol{h}|/m_s = 0.05$ and energy is minimized at $\theta_m = 86^\circ$ (dashed line). (b) Field magnitude is $|\boldsymbol{h}|/m_s = 0.4$ and energy is minimized at $\theta_m = 72^\circ$ (dashed line).

As a simple example, for an applied field direction defined by $\phi_h = 0$ and $\theta_h = 30^\circ$, we compute the magnetization of a square plate with values of c_{s1} and c_{s2} equal to demagnetization factors (n_r and n_a) [33], respectively, of an oblate ellipsoid with major to minor axis ratio of 20 (the square head of the microswimmer in Ref. [27] has a length to thickness ratio of 22.5). The value of c_{s3} is not relevant since $\phi_h = 0$. We also know that ϕ_m should be zero due to the symmetry of the square around its x axis. Hence Eq. (C1) is simplified and $|\boldsymbol{m}|$ becomes

$$|\boldsymbol{m}| = \frac{|\boldsymbol{h}| \cos(\theta_m - \theta_h)}{c_{s2} \cos^2(\theta_m) + c_{s1} \sin^2(\theta_m)}. \tag{C4}$$

Figure 7 shows energy values plotted for two field magnitudes with different θ_m when the energy is computed with $|\boldsymbol{m}| = m'$, $|\boldsymbol{m}| = m_s$, and $|\boldsymbol{m}| = \tilde{m}$; the latter is the actual value of energy. Magnetization due to the applied field then corresponds to the point where energy is minimized. We

FIG. 8. Surface discretization of microswimmer with thin square plate head. To scale, 894 total discretization points.

see that for smaller field magnitudes, the magnetization is unsaturated and tends to be closer to the easy axis and for higher field magnitudes it is saturated and tends to get closer to the field.

Geometry and mobility matrix for a helical microswimmer with a square head. The microswimmer in Ref. [27] has a tail which is a left-handed helical ribbon with 4.5 turns, helical length of 38 μm, helical radius of 1.4 μm, and made of a trilayer of InGaAs/GaAs/Cr with a ribbon width of 1.8 μm and thickness of 32 nm. The tail is attached to a $4.5 \times 4.5 \times 0.2$ μm^3 thin square head made of Cr/Ni/Au such that the helical axis is aligned with one of the square's diagonals. To calculate the mobility matrix, we discretized the surface of the six faces of the square head with dimensions reported in the paper by putting equally distanced points on each surface. We discretized the helical ribbon tail with one layer of Stokeslets as shown in Fig. 8. We put equally spaced points on lines parallel to the helical axis. Each line has length $w_r \cos(\pi/4)$ where w_r is the ribbon width, and the distance between neighboring lines is equal to the distance between two neighboring points on a line.

The regularization parameters used for the head and the tail are equal to the distance between two neighboring points on the head and the distance between two neighboring lines on the tail, respectively. We set the distance between two adjacent points of the head to be 2.5 times bigger than that of the tail and we increase the number of discretization points by decreasing the distance of adjacent points on the tail. Similarly to the case of the ellipsoidal microswimmer, we ensure convergence of mobility values by increasing the number of points until the percentage change of $||\boldsymbol{K}||$, $||\boldsymbol{C}||$, and $||\boldsymbol{M}||$ in the last three computations is less than 1%.

For our final simulations the ribbon tail has 9525 points, the square head has 722 points, and the values for submatrices $\boldsymbol{K}$, $\boldsymbol{C}$, and $\boldsymbol{M}$ are

$$\boldsymbol{K} = \begin{bmatrix} 1.9637 & 0.0034 & -0.0092 \\ 0.0034 & 1.1285 & -0.0487 \\ -0.0092 & -0.0487 & 1.7136 \end{bmatrix} \times 10^7 \text{ N}^{-1}\,\text{s}^{-1}\,\text{m}, \tag{C5}$$

$$\boldsymbol{C} = \begin{bmatrix} -0.0046 & 1.1482 & -0.06260 \\ -0.0411 & -0.1736 & -0.0156 \\ 0.5940 & -0.0782 & -0.0025 \end{bmatrix} \times 10^{12} \text{ N}^{-1}\,\text{s}^{-1}, \tag{C6}$$

$$\boldsymbol{M} = \begin{bmatrix} 0.0379 & -0.0087 & -0.0006 \\ -0.0087 & 1.3652 & 0.0344 \\ -0.0006 & 0.0344 & 0.0412 \end{bmatrix} \times 10^{18} \text{ N}^{-1}\,\text{s}^{-1}\,\text{m}^{-1}. \tag{C7}$$

This mobility matrix can be checked since the ratio $|C_{22}/M_{22}|$ [Eq. (1) of the text] should be equal to the slope of the velocity-frequency plots in Fig. 4(b). This slope is reported to be 1.1×10^{-7} m [27], and the value that we computed for $|C_{22}/M_{22}|$ is 1.27×10^{-7} m.

Discussion of the implied m_s value for microswimmer with square head. Here we argue that the implied value for m_s found in our model of the microswimmer with a thin square head is reasonable. The square head of the microswimmer in [27] is a trilayer alloy made up of Cr/Ni/Au with thickness of 10/180/10 nm, while it has a trilayer tail of InGaAs/GaAs/Cr with thickness of 11/16/15 nm. Nickel is a soft magnet with a saturation magnetization $m_s \approx 4.9 \times 10^5$ A m^{-1} while chromium is an antiferromagnetic metal and all the rest of the metals used in the head and tail are diamagnetic.

The value of m_s found in our fit ($m_s \approx 2 \times 10^4$ A m^{-1}) is much lower than that of nickel, but the trilayer structure could significantly affect m_s. We were not able to compute the saturation

magnetization of this exact trilayer structure, but the saturation magnetizations of a number of similar structures have been reported. Reference [52] reports m_s values of a series of biaxially textured $Ni_{1-x}Cr_x$ materials, in which increasing x decreases m_s such that $x = 7\%$ results in a m_s almost 2.5 times smaller than that of nickel, while $x = 13\%$ results in a m_s 144 times smaller than that of nickel. Reference [53] reports m_s values for biaxially textured substrates of Ni/W, in which increasing the percentage of W decreases m_s, and they estimate m_s to become zero for $Ni_{91}W_9$. Reference [54] reports m_s values for Ni/Au superlattices with bilayer thicknesses less than 5 nm, in which decreasing the thickness of the Ni layer decreases m_s. Based on these reports and considering the amount of chromium (35% in head and tail combined) and the diamagnetic materials of the head and tail, we believe that $m_s = 2 \times 10^4\ \mathrm{A\,m^{-1}}$ is not an unreasonable value for the saturation magnetization of the swimmer in [27].

[1] C. Bechinger, R. Di Leonardo, H. Löwen, C. Reichhardt, G. Volpe, and G. Volpe, Active particles in complex and crowded environments, Rev. Mod. Phys. **88**, 045006 (2016).

[2] J. Li, B. Esteban-Fernández de Ávila, W. Gao, L. Zhang, and J. Wang, Micro/nanorobots for biomedicine: Delivery, surgery, sensing, and detoxification, Sci. Robot. **2**, eaam6431 (2017).

[3] W. F. Paxton, K. C. Kistler, C. C. Olmeda, A. Sen, S. K. St. Angelo, Y. Cao, T. E. Mallouk, P. E. Lammert, and V. H. Crespi, Catalytic nanomotors: Autonomous movement of striped nanorods, J. Am. Chem. Soc. **126**, 13424 (2004).

[4] A. Aubret, M. Youssef, S. Sacanna, and J. Palacci, Targeted assembly and synchronization of self-spinning microgears, Nat. Phys. **14**, 1114 (2018).

[5] R. Dreyfus, J. Baudry, M. L. Roper, M. Fermigier, H. A. Stone, and J. Bibette, Microscopic artificial swimmers, Nature (London) **437**, 862 (2005).

[6] P. Tierno, R. Golestanian, I. Pagonabarraga, and F. Sagués, Controlled Swimming in Confined Fluids of Magnetically Actuated Colloidal Rotors, Phys. Rev. Lett. **101**, 218304 (2008).

[7] H.-R. Jiang, N. Yoshinaga, and M. Sano, Active Motion of a Janus Particle by Self-Thermophoresis in a Defocused Laser Beam, Phys. Rev. Lett. **105**, 268302 (2010).

[8] W. Wang, L. A. Castro, M. Hoyos, and T. E. Mallouk, Autonomous motion of metallic microrods propelled by ultrasound, ACS Nano **6**, 6122 (2012).

[9] A. Bricard, J.-B. Caussin, N. Desreumaux, O. Dauchot, and D. Bartolo, Emergence of macroscopic directed motion in populations of motile colloids, Nature (London) **503**, 95 (2013).

[10] H. Karani, G. E. Pradillo, and P. M. Vlahovska, Tuning the Random Walk of Active Colloids: From Individual Run-and-Tumble to Dynamic Clustering, Phys. Rev. Lett. **123**, 208002 (2019).

[11] E. Lauga and T. R. Powers, The hydrodynamics of swimming microorganisms, Rep. Prog. Phys. **72**, 096601 (2009).

[12] E. B. Steager, M. S. Sakar, D. H. Kim, V. Kumar, G. J. Pappas, and M. J. Kim, Electrokinetic and optical control of bacterial microrobots, J. Micromech. Microeng. **21**, 035001 (2011).

[13] Y. Alapan, O. Yasa, O. Schauer, J. Giltinan, A. F. Tabak, V. Sourjik, and M. Sitti, Soft erythrocyte-based bacterial microswimmers for cargo delivery, Sci. Robot. **3**, eaar4423 (2018).

[14] A. Ghosh and P. Fischer, Controlled propulsion of artificial magnetic nanostructured propellers, Nano Lett. **9**, 2243 (2009).

[15] L. Zhang, J. J. Abbott, L. Dong, B. E. Kratochvil, D. Bell, and B. J. Nelson, Artificial bacterial flagella: Fabrication and magnetic control, Appl. Phys. Lett. **94**, 064107 (2009).

[16] P. J. Vach, P. Fratzl, S. Klumpp, and D. Faivre, Fast magnetic micropropellers with random shapes, Nano Lett. **15**, 7064 (2015).

[17] J. J. Abbott, K. E. Peyer, M. C. Lagomarsino, L. Zhang, L. Dong, I. K. Kaliakatsos, and B. J. Nelson, How should microrobots swim? Int. J. Robot. Res. **28**, 1434 (2009).

[18] A. Ghosh, D. Paria, H. J. Singh, P. L. Venugopalan, and A. Ghosh, Dynamical configurations and bistability of helical nanostructures under external torque, Phys. Rev. E **86**, 031401 (2012).

[19] Y. Man and E. Lauga, The wobbling-to-swimming transition of rotated helices, Phys. Fluids **25**, 071904 (2013).
[20] A. Acemoglu and S. Yesilyurt, Effects of geometric parameters on swimming of micro organisms with single helical flagellum in circular channels, Biophys. J. **106**, 1537 (2014).
[21] U. K. Cheang, F. Meshkati, D. Kim, M. J. Kim, and H. C. Fu, Minimal geometric requirements for micropropulsion via magnetic rotation, Phys. Rev. E **90**, 033007 (2014).
[22] F. Meshkati and H. C. Fu, Modeling rigid magnetically rotated microswimmers: Rotation axes, bistability, and controllability, Phys. Rev. E **90**, 063006 (2014).
[23] K. I. Morozov and A. M. Leshansky, Dynamics and polarization of superparamagnetic chiral nanomotors in a rotating magnetic field, Nanoscale **6**, 12142 (2014).
[24] K. I. Morozov and A. M. Leshansky, The chiral magnetic nanomotors, Nanoscale **6**, 1580 (2014).
[25] F. A. Godínez, L. Koens, T. D. Montenegro-Johnson, R. Zenit, and E. Lauga, Complex fluids affect low-Reynolds number locomotion in a kinematic-dependent manner, Exp. Fluids **56**, 97 (2015).
[26] H. C. Fu, M. Jabbarzadeh, and F. Meshkati, Magnetization directions and geometries of helical microswimmers for linear velocity-frequency response, Phys. Rev. E **91**, 043011 (2015).
[27] L. Zhang, J. J. Abbott, L. Dong, K. E. Peyer, B. E. Kratochvil, H. Zhang, C. Bergeles, and B. J. Nelson, Characterizing the swimming properties of artificial bacterial flagella, Nano Lett. **9**, 3663 (2009).
[28] D. Jiles, *Introduction to Magnetism and Magnetic Materials*, 3rd ed. (CRC Press, 2015).
[29] P. J. Vach, N. Brun, M. Bennet, L. Bertinetti, M. Widdrat, J. Baumgartner, S. Klumpp, P. Fratzl, and D. Faivre, Selecting for function: Solution synthesis of magnetic nanopropellers, Nano Lett. **13**, 5373 (2013).
[30] K. I. Morozov, Y. Mirzae, O. Kenneth, and A. M. Leshansky, Dynamics of arbitrary shaped propellers driven by a rotating magnetic field, Phys. Rev. Fluids **2**, 044202 (2017).
[31] A. Codutti, F. Bachmann, D. Faivre, and S. Klumpp, Bead-based hydrodynamic simulations of rigid magnetic micropropellers, Front. Robot. AI **5**, 109 (2018).
[32] Y. Mirzae, O. Dubrovski, O. Kenneth, K. I. Morozov, and A. M. Leshansky, Geometric constraints and optimization in externally driven propulsion, Sci. Robot. **3**, eaas8713 (2018).
[33] J. J. Abbott, O. Ergeneman, M. P. Kummer, A. M. Hirt, and B. J. Nelson, Modeling magnetic torque and force for controlled manipulation of soft-magnetic bodies, IEEE Trans. Robot. **23**, 1247 (2007).
[34] J. A. Osborn, Demagnetizing factors of the general ellipsoid, Phys. Rev. **67**, 351 (1945).
[35] R. Cortez, The method of regularized Stokeslets, SIAM J. Sci. Comput. **23**, 1204 (2001).
[36] K. Samsami, S. A. Mirbagheri, F. Meshkati, and H. C. Fu, Stability of soft magnetic helical microrobots, Fluids **5**, 19 (2020).
[37] F. Hagedorn and E. Gyorgy, Magnetic-shape anisotropy in polygonal prisms, J. Appl. Phys. **39**, 995 (1968).
[38] J. Crangle and G. M. Goodman, The magnetization of pure iron and nickel, Proc. R. Soc. London A **321**, 477 (1971).
[39] K.-J. Cohen, B. Y. Rubinstein, O. Kenneth, and A. M. Leshansky, Unidirectional Propulsion of Planar Magnetic Nanomachines, Phys. Rev. Appl. **12**, 014025 (2019).
[40] F. Bachmann, K. Bente, A. Codutti, and D. Faivre, Using Shape Diversity on the Way to Structure-Function Designs for Magnetic Micropropellers, Phys. Rev. Appl. **11**, 034039 (2019).
[41] A. W. Mahoney, N. D. Nelson, K. E. Peyer, B. J. Nelson, and J. J. Abbott, Behavior of rotating magnetic microrobots above the step-out frequency with application to control of multi-microrobot systems, Appl. Phys. Lett. **104**, 144101 (2014).
[42] J. J. Abbott and H. C. Fu, Controlling homogeneous microrobot swarms in vivo using rotating magnetic dipole fields, in *Robotics Research: 18th International Symposium ISRR, Springer Proceedings in Advanced Robotics* (Springer, 2017), Vol. 10, p. 3.
[43] C. E. Sing, L. Schmid, M. F. Schneider, T. Franke, and A. Alexander-Katz, Controlled surface-induced flows from the motion of self-assembled colloidal walkers, Proc. Natl. Acad. Sci. USA **107**, 535 (2010).
[44] T. O. Tasci, P. S. Herson, K. B. Neeves, and D. W. M. Marr, Surface-enabled propulsion and control of colloidal microwheels, Nat. Commun. **7**, 10225 (2016).
[45] M. Driscoll, B. Delmotte, M. Youssef, S. Sacanna, A. Donev, and P. Chaikin, Unstable fronts and motile structures formed by microrollers, Nat. Phys. **13**, 375 (2017).

[46] Y. Alapan, B. Yigit, O. Beker, A. F. Demirors, and M. Sitti, Shape-encoded dynamic assembly of mobile micromachines, Nat. Mater. **18**, 1244 (2019).
[47] T. A. Waigh, Microrheology of complex fluids, Rep. Prog. Phys. **68**, 685 (2005).
[48] J. Dobson, Remote control of cellular behavior with magnetic nanoparticles., Nat. Nanotechnol. **3**, 139 (2008).
[49] Y. Cheng, M. E. Muroski, D. C. Petit, R. Mansell, T. Vemulkar, R. A. Morshed, Y. Han, I. V. Balyasnikova, C. M. Horbinski, X. Huang, L. Zhang, R. P. Cowburn, and M. S. Lesniak, Rotating magnetic field induced oscillation of magnetic particles for in vivo mechanical destruction of malignant glioma, J. Controlled Release **223**, 75 (2016).
[50] B. Wang, K. F. Chan, J. Yu, Q. Wang, L. Yang, P. W. Y. Chiu, and L. Zhang, Reconfigurable swarms of ferromagnetic colloids for enhanced local hyperthermia, Adv. Funct. Mater. **28**, 1705701 (2018).
[51] B. Steinberger, N. Petersen, H. Petermann, and D. G. Weiss, Movement of magnetic bacteria in time-varying magnetic fields, J. Fluid Mech. **273**, 189 (1994).
[52] J. R. Thompson, A. Goyal, D. K. Christen, and D. M. Kroeger, Ni-Cr textured substrates with reduced ferromagnetism for coated conductor applications, Phys. C (Amsterdam) **370**, 169 (2002).
[53] H. Sakamoto, Y. Nagasu, Y. Ohashi, R. Nakasaki, M. Mimura, and A. Nakai, Development of textured substrates with low magnetism, Phys. C (Amsterdam) **463-465**, 600 (2007).
[54] J. R. Childress, C. L. Chien, and A. F. Jankowski, Magnetization, Curie temperature, and magnetic anisotropy of strained (111) Ni/Au superlattices, Phys. Rev. B **45**, 2855 (1992).